

## Validation of materials-informed digital twin: Mapping residual strains in HSLA steel weldment using high energy X-rays



Charles R. Fisher<sup>a,\*</sup>, Kelly E. Nygren<sup>b</sup>, Armand J. Beaudoin<sup>b</sup>

<sup>a</sup> Naval Surface Warfare Center – Carderock Division (NSWCCD), 9500 MacArthur Blvd, West Bethesda, MD 20817, USA

<sup>b</sup> Cornell High Energy Synchrotron Source (CHESS), 161 Synchrotron Drive, Ithaca, NY 14853, USA

### ARTICLE INFO

#### Keywords:

FEA  
Residual stress  
Synchrotron diffraction  
SYSWELD  
Welding

### ABSTRACT

The shipbuilding industry has placed an emphasis on establishing digital twin prototypes to advance computational lifecycle analysis capabilities. However, material processing data is not currently included in simulations for structural performance, which could lead to inaccuracies. Integrated Computational Materials Engineering (ICME) techniques yield a path to solving this problem through linking digital information across multiple length scales in order to minimize the time and cost of physical testing needed for validation. This paper details the initial work of a larger materials-informed digital twin effort seeking to validate the need for fabrication inclusion in lifecycle analysis. First, the selection and fabrication of the “sister sample” specimens used for physical validation from a single plate of HSLA-100 steel. Second, the finite-element analysis (FEA)-based welding simulations of the reinforced dog-bone weldment. Third, comparison of predicted strain data from FEA simulations to two-dimensional (2D) strain maps using energy dispersive diffraction (EDD) techniques at the Cornell High-Energy Synchrotron Source (CHESS). The results showed high correlation between the measured EDD data and the FEA predictions, particularly for the high strain ( $>0.0015$ ) fields of first principle strain vectors measured parallel to each welding pass. This computational validation is the first step towards validating the materials-informed digital twin method for increasing accuracy of structural analysis and fatigue lifecycle evaluation.

### 1. Introduction

There is a desire to establish digital twin prototypes for assets across the shipbuilding industry. These “digital twins” are a digital representation of a physical component, assembly, or product and will be used for lifecycle analysis and product management. However, material processing data, particularly residual stress distribution, is unable to be currently included for lifecycle analysis due to limitations with current computational toolsets. This represents a major hurdle to digital twin development, as residual stress induced from material processing and structural fabrication can cause severe degradation of structural performance [1]. Both Webster and Ezeilo [2] and Barsoum and Barsoum [3] found that proper structural fatigue life predictions require precise residual stress distribution knowledge. However, quantification of accumulated stress and its distribution throughout the shipbuilding process is not well characterized [4], especially for non-welding-related processing.

The Integrated Computational Materials Engineering (ICME) paradigm is “...the integration of materials information, captured in

computational tools, within engineering product performance analysis and manufacturing-process simulation” [5]. ICME programs have evolved to solve major manufacturing issues, including: 1) decreasing material development time, 2) ensuring manufacturing competitiveness, and 3) increasing technological advantage. Specifically, ICME techniques have shown the potential to reduce the cost and time to design and deploy materials [6]. However, the strength of the ICME paradigm comes from linking digital information across multiple length scales in order to minimize the time and cost of physical testing, which has been a difficult undertaking.

Across the shipbuilding industry, there are numerous groups working on extremely complex simulations ranging from structural design to material processing. However, due to the highly specialized nature of the technical expertise, the varied groups are not easily able to collaborate across digital tools. Therefore, to meet the materials-informed digital twin objective, a project was initiated to leverage ICME techniques in order to computationally link disparate software codes while validating the digital data with physical testing. This project links finite-element analysis (FEA) tools across plate processing, shape cutting and

\* Corresponding author.

E-mail address: [charles.r.fisher1@navy.mil](mailto:charles.r.fisher1@navy.mil) (C.R. Fisher).

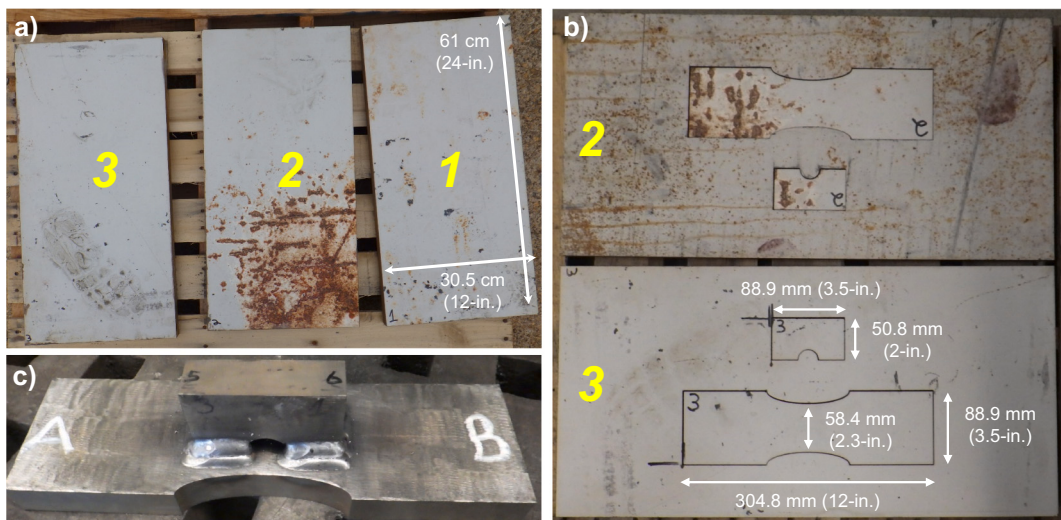


**Fig. 1.** The 25.4 mm (1-in.) thick plate of HSLA-100 steel showing: a) the three 61 cm by 30.5 cm (2-ft by 1-ft) sub-plates, b) Plate #2 and #3 after the second water-jet cutting process to produce the dog-bone and arch shapes, and c) post-welding to produce the final component, Specimen #3.

machining, welded fabrication, and structural performance. The FEA simulations were paired with physical measurement for verification and validation (V&V) of strain evolution in the final welded assembly. A digital comparison of the fatigue life for the part-level model both with and without fabrication information (*i.e.*, residual stress from processing, machining, and welding) is essential to understanding how fabrication affects performance on larger prototypes and assets. Again, V&V techniques will be used to compare the simulation results with physical measurements. This novel simulation linkage across fabrication steps to mechanical performance will enable lifecycle and digital twin analysis for assets across the shipbuilding industry.

High-energy X-ray measurements were utilized to validate the simulation results and establish the digital thread between material processing FEA tools and structural FEA tools in order to inform how fabrication affects resultant lifecycle performance. The use of high-energy X-rays provided a powerful tool to measure not only surface strains, but also resolve strain gradients at depth across the various components investigated in the project. This was critical to verify the computational models across various fabrication steps as both machining and welding induces modification of through-thickness stresses. There are other techniques to measure residual stresses as validation for FEA simulations, such as the contour method, hole drilling, or neutron diffraction. Several studies have been conducted to show similar results across the contour method and X-ray diffraction [7,8], hole drilling and X-ray diffraction [9], contour and neutron diffraction [10], and across the contour method, X-ray diffraction, and neutron diffraction [11,12]. However, neither the contour method nor hole drilling were considered for this study due to being destructive by nature. Follow-on submissions are planned to compare this paper's FEA prediction and X-ray measurement results to neutron diffraction measurements once the data are analyzed.

The following effort embraced experimental measurement with concomitant model validation: mapping of a subset of strain components provides validation of a weld process model. The expected state of residual stress does not follow from the measurement, but rather from the FEA model prediction. It was the spatial resolution of the experimental mapping that was key to validation. A prototype for the present effort was shown previously by Mach et al. [13]. Recent efforts have extended this general approach to a multiple-pass fillet weld model in comparison to neutron diffraction analysis and the contour method for V&V [14].

For HSLA-100, the material of concern with regard to the present effort, residual stress in quenched 60.75 mm (2.4-in.) thick HSLA-100 plate have been measured by the contour method by Prime [15]. The

measurement was complemented by an FEA simulation to derive stress relaxation associated with sample removal from the parent plate. An expected pattern of an in-plane tensile component of stress balanced by compressive stresses on the top and bottom surfaces was found. The maximum values were roughly 200 MPa in the tension and compression regions. The relation of residual stress to texture and subsequent impact on residual stress determination in HSLA-100 was explored for variations in thermomechanical treatment by Bahadur et al. [16]. They also measured surface residual stress magnitudes around 200 MPa, but noted that the surface of the plate was in tension from the quenching process, highlighting the need to understand all steps in the fabrication process. Insight into weld thermal cycles of HSLA-100 was developed through characterization and simulation of microstructure combined with measurement of mechanical properties by Duch and Dupont [17].

This paper details three stages within the greater materials-informed digital twin effort at NSWCCD. First, it details the selection and fabrication of the three HSLA-100 steel specimens. Second, the welding simulations and analysis of the final welded component. Lastly, the comparison of predicted FEA data to two-dimensional (2D) strain maps produced at CHESS. It should be noted that throughout the paper, when referencing strain (either measurement or simulations), this is referring to total strain unless otherwise specified.

## 2. Technical approach

### 2.1. Specimen fabrication

The selected plate used for all specimens within this project was nominally a 25.4 mm (1-in.) thick plate of high-strength low alloy (HSLA)-100 steel. The HSLA-100 plate conformed to the NAVSEA Technical Publication 300 Composition 1 specifications [18], which requires a minimum yield strength of 690 MPa (100 ksi). The chemical composition of the base material was confirmed at NSWCCD using glow discharge atomic emission spectrometry (GD-AES) on a Leco GDS900 in accordance with ASTM E415 [19] for all elements except carbon and sulfur; these elements were analyzed at NSWCCD on a Leco CS844 using a combustion technique in accordance with ASTM E1019 [20]. The mechanical properties of the plate were confirmed by testing at Westmoreland Mechanical Testing and Research, Inc. in Youngstown, PA using ASTM A370 [21].

#### 2.1.1. Shape cutting and welded fabrication

The HSLA-100 plate had an original approximate width and length of

**Table 1**

Comparison of steel material properties at room temperature.

Material	Thermal conductivity		Yield strength	
	W/m·K	BTU/h·ft·°F	MPa	ksi
HSLA-100 [18,29]	35.6	20.6	>690	>100
TRIP 700Z [26]	34.0	19.7	700	101.5

1.52 m by 4.27 m (5-ft by 14-ft). It was not a newly procured plate, but instead selected from previous stock to ensure weathering of the plate was included in the analysis, mimicking processes at a shipyard. A detailed description of the entire “sister sample” fabrication process can be found in the Supplementary information. Instead of having a single specimen investigated at various points throughout the fabrication cycle, which would have increased the time requirements and cycle times for strain measurements, the sister samples were used to mimic each step in the fabrication process during a single session at a beamline.

Fig. 1 shows the three sub-plates cut to a size of 61 cm by 30.5 cm (2-ft by 1-ft), the second round of water-jet cutting to achieve the dog-bone and arch shapes, as well as the final weldment, referred to as Specimen #3 throughout. The final shape of Specimen #3 was determined to ensure it could be tested in a fatigue lifecycle scenario at a future date. In addition, the reinforcement arch welded in six locations (four longitudinally, two transverse) to the dog-bone shape increased the likelihood of high longitudinal and transverse strain gradients would be present post-welding.

Representative weld beads using similar parameters to those used for the fabrication of Specimen #3 were also prepared. The representative Tee-joint weld scenarios included: 1) GTAW root pass only, 2) GTAW root pass with single GMAW cover pass, and 3) GTAW root pass with three GMAW cover passes. Each representative joint was cross-sectioned, mounted, polished to a final grit of 0.04 μm using colloidal silica, and etched with fresh 2% Nital solution.

## 2.2. Computational simulation

Specimen #3 was computationally simulated using *SYSWELD*, a

commercially-available welding-specific finite-element code from ESI. Simulations were set-up on the *Visual Weld* (version 14.5) module and run using the *SYSWELD* solver (version 2019.0). Solid elements and transient heat source simulation using a Goldak heat source model [22] were used analyze the distortion and stress evolution from the welding process. The V&V techniques utilized for the simulation are described in the American Welding Society (AWS) A9.5 *Guide for Verification and Validation in Computational Weld Mechanics* [23]. The cross-sections from the representative Tee-joints ensured correct sizing for each weld pass. An average welding arc efficiency of 67% was used to mimic the GTAW passes, whereas it was 85% for the GMAW passes in accordance with reference [24]. The other welding parameters mimicked that of the physical specimen fabrication, but used average values for the welding parameters. The radiative and convective losses were calculated using a radiation emissivity ( $\epsilon_0$ ) of 0.8 and convective heat transfer coefficient ( $h_c$ ) of 25 W/m<sup>2</sup>/K, the default values from the *Visual Weld* module software for a “free air cooling” scenario [25]. A more detailed description of the entire computational simulation process can be found in the Supplementary information.

As noted in the previous section, the frame was fabricated of HSLA-100 steel with an ER100-s filler metal. However, the *SYSWELD* software did not have a material database for either of these materials at the time this project was conducted. Therefore, a material called ‘TRIP 700Z’ [26] was used for both the plate and filler metal in all simulations. Table 1 shows a comparison between the typical thermal conductivity and yield strength values for the base metal materials at 25 °C (77 °F). Note the highly similar thermal and strength properties between the HSLA-100 and TRIP 700Z steels. Future analysis will be completed to determine the effect of using this replacement material after a pedigree, temperature-dependent material property database for HSLA-100 is generated at NSWCCD.

## 2.3. Strain analysis

Measurements were performed on the structural materials beamline (SMB) at CHESS. Energy dispersive diffraction (EDD) was carried out using polychromatic (50–200 keV) x-rays. An overview of the experimental set-up is shown in Fig. 2. For these measurements, a single-

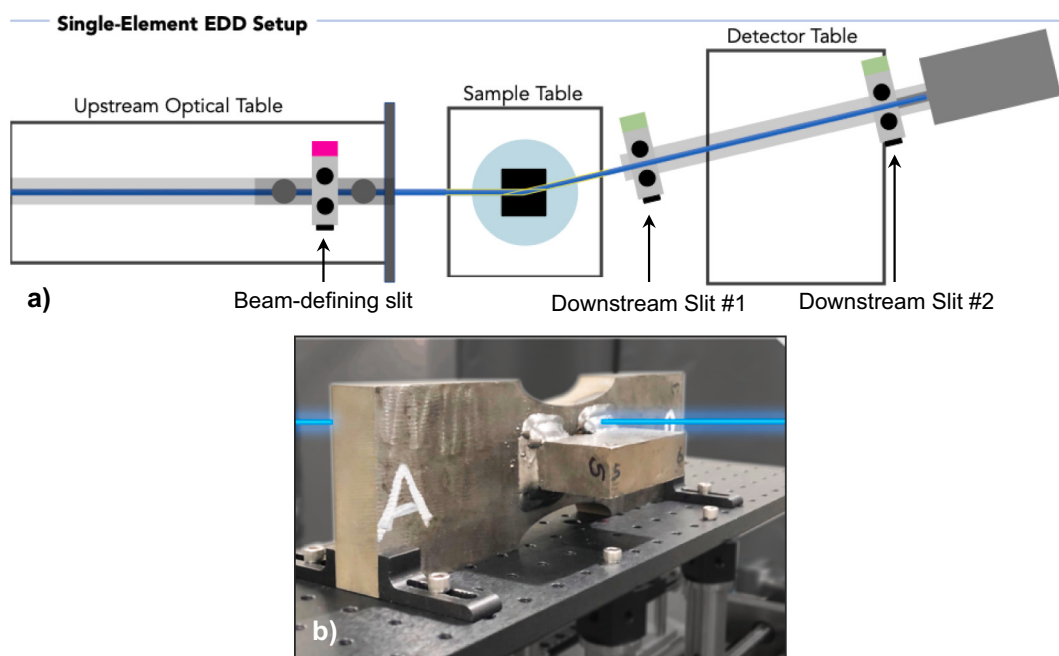


**Fig. 2.** a) Overview of the EDD experimental set-up at CHESS and b) close-up of Specimen #3 on the sample table in one configuration with the direct beam-path (blue line) drawn for clarity. (For interpretation of the references to color in this figure legend, the reader is referred to the web version of this article.)

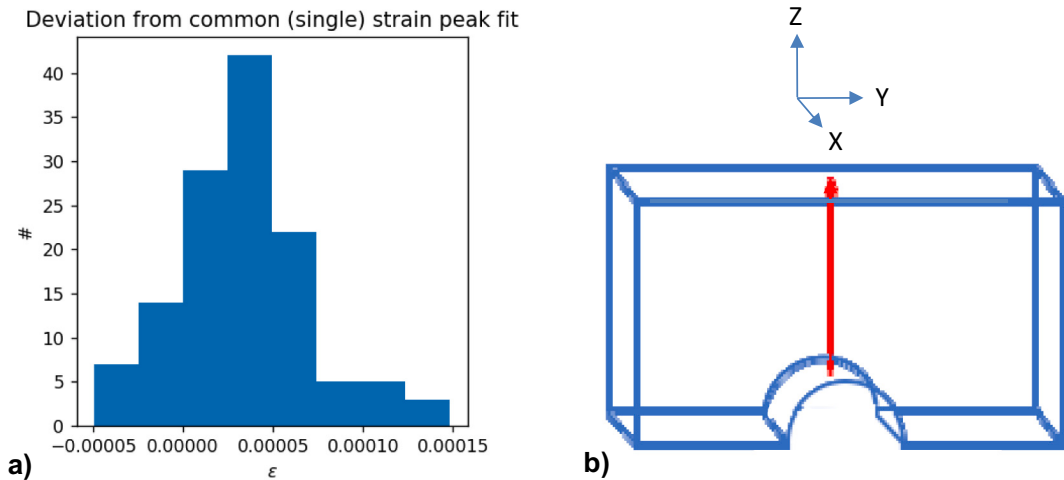


**Fig. 3.** a) Distribution of difference between fit for  $\epsilon_{yy}$  component, taking a common strain to fit peaks and average of least squares solution with distinct strain evaluated for each peak. b) Geometry of calibration scan on the water-jet cut but un-welded reinforcement arch from Plate #2.

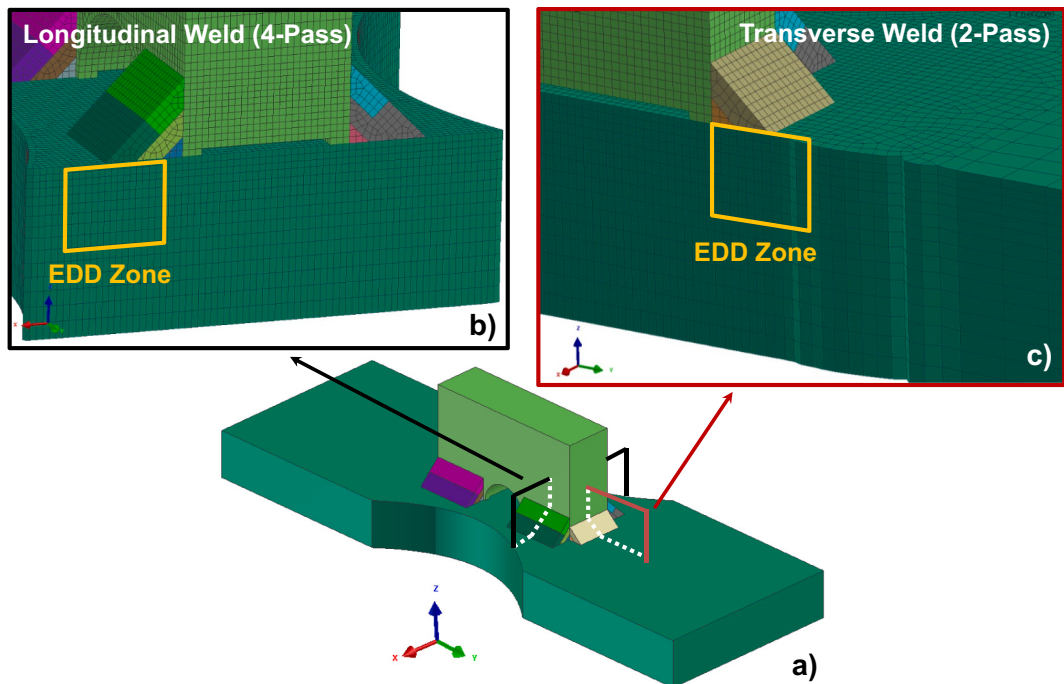


**Fig. 4.** Image of the a) CAD model showing the locations of the EDD measurement zones below the b) longitudinal and c) transverse weld joints.

element Canberra GL-0055 energy resolved detector was used and placed on a down-stream optical path (also referred to in this report as the detector arm) in the horizontal plane at a 20° angle of 7.82026. The diffraction volume was defined by: a) the beam-defining slit upstream of the sample [0.2 mm (0.008-in.) horizontal by 0.5 mm (0.020-in.) vertical]; and b) two slits on the downstream detector arm with a separation distance of ~1420 mm (55.9-in.) when the first slit was 718 mm (28.3-in.) away from the sample. The diffraction volume in the horizontal plane had a through-thickness full-width at half-maximum (FWHM) of 1.08 mm (0.04-in.). The horizontal slit size was critical to establishing the through-thickness resolution, while the relatively larger vertical slit spacing increased the diffraction volume and decreased collection time for this relatively thick steel plate.

For calculating the strains, the true strain was taken as:

$$\varepsilon = \ln\left(\frac{d^{(i)}}{d_0^{(i)}}\right) \quad (1)$$

where  $d_0^{(i)}$  is the reference and  $d^{(i)}$  is the elastically-deformed lattice spacing for reflection. Introducing Bragg's Law,  $\lambda = 2d^{(i)}\sin\hat{\theta}$ , where  $\lambda$  is the wavelength and  $\hat{\theta}$  is the fixed angle from the EDD geometry, yields:

$$\varepsilon = \ln\left(\frac{d_0^{(i)}\sin\hat{\theta}}{\lambda^{(i)}\sin\hat{\theta}}\right) \quad (2)$$

Taking  $E^{(i)} = 12.398 / \lambda^{(i)}$ , where  $E^{(i)}$  is the energy and 12.398 is a value generated by multiplying Plank's constant by the speed of light, and simplifying Eq. (2) yields:

**Table 2**  
Chemical composition of HSLA-100 plate (wt%).

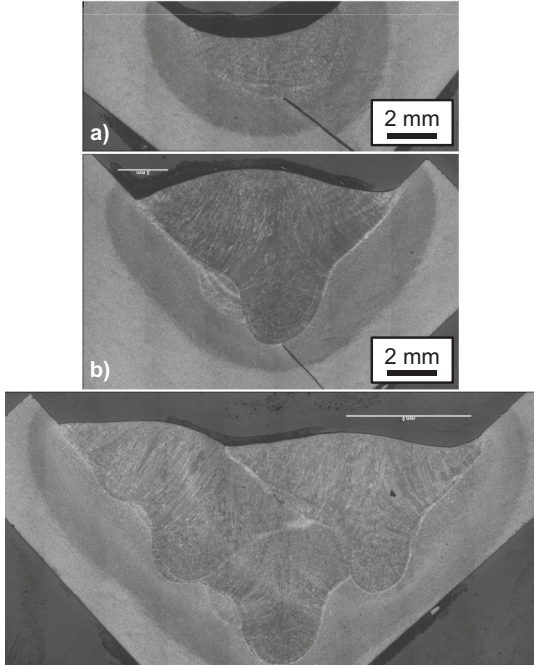
Type	C	Mn	Si	Ni	Cr	Mo	Cu	P	S	Nb	Al	Ti	V	Sn	Fe
Measured	0.05	0.88	0.24	1.71	0.60	0.32	1.15	0.008	0.003	0.03	0.019	0.00	0.022	Bal.	Bal.
Specification	<0.06	0.75–1.15	<0.40	1.50–2.00	0.45–0.75	0.30–0.55	1.00–1.30	<0.020	<0.004	0.02–0.06	>0.010	<0.02	<0.03	<0.030	<0.030

**Table 3**  
Mechanical properties of HSLA-100 plate.

Longitudinal specimen	#1	#2	#3	#4	Avg. $\pm 1\sigma$
Elastic modulus (GPa)	202.7	195.8	200.6	201.3	200.1 $\pm$ 3.0
Yield strength (MPa)	717.7	704.6	711.5	703.3	709.3 $\pm$ 6.7
Tensile strength (MPa)	778.4	772.2	775.0	768.8	773.6 $\pm$ 4.1
Elongation (%)	25	25	25	25	25.0 $\pm$ 0

Transverse specimen	#5	#6	#7	#8	Avg. $\pm 1\sigma$
Elastic modulus (GPa)	211.7	204.8	206.2	204.1	206.7 $\pm$ 3.4
Yield strength (MPa)	707.4	725.3	710.2	717.1	715.0 $\pm$ 8.0
Tensile strength (MPa)	772.9	783.9	772.2	781.2	777.6 $\pm$ 5.9
Elongation (%)	25	25	25	25	25.0 $\pm$ 0



**Fig. 5.** Representative cross-sections of the different joint conditions for weld bead size comparison of the a) GTAW root pass, b) GTAW root pass and GMAW cover pass, and c) GTAW root pass and three GMAW cover passes.

$$\varepsilon = \ln \left( \frac{E_0^{(i)}}{E^{(i)}} \right) \quad (3)$$

Rearranging Eq. (3), the energy based on the instantaneous value of the lattice strain ( $\varepsilon$ ) is then:

$$E^{(i)} = E_0^{(i)} \exp(\varepsilon^{(i)}) \quad (4)$$

Multiple peaks were fit simultaneously, using the least squares routine from the SciPy optimization library [27]. Optimized parameters included the peak center intensity (as energy) and shape. Calculation of the residual draws peak evaluation routines from hexrd [28]; a Gaussian peak profile was taken in the present work. A linear background correction was included and bounds are prescribed for the peak shape, such that parameters associated with a relatively weak peak are restricted from contributing to the overall background correction. Three progressive least squares optimizations were performed as described below:

- Initial optimization using a common strain for all peaks,  $i$ , such that:  
 $\varepsilon^{(i)} = \bar{\varepsilon}$ .

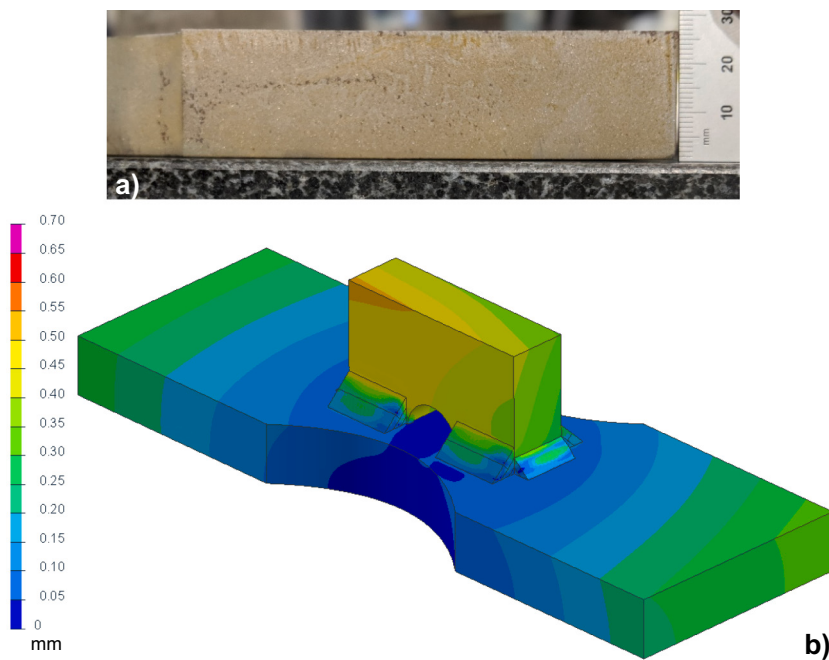


**Fig. 6.** Distortion analysis showing a) image of the slight curvature (less than 1 mm [0.04-in.]) found in dog-bone shape portion of Specimen #3 post-welding compared to b) SYSWELD image of the final predicted distortion state of the weldment after the completion of welding and the cooling period to bring the piece back to room temperature.

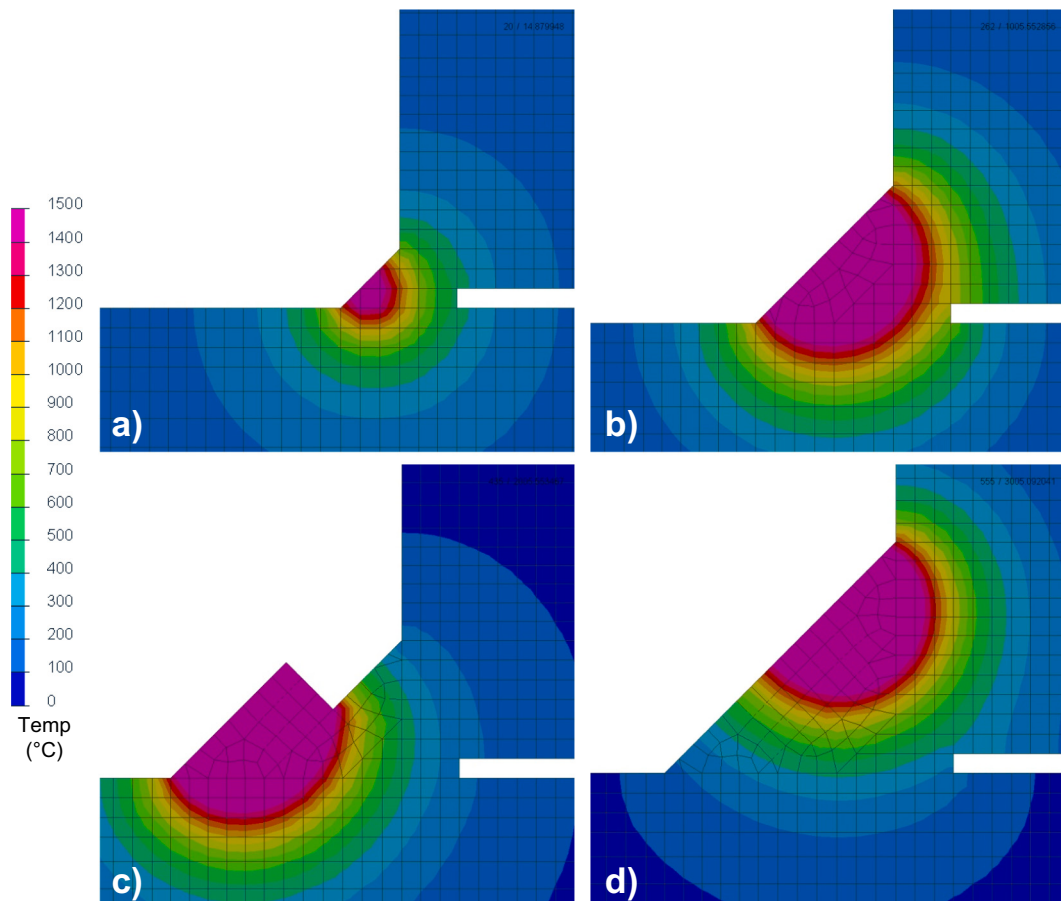


**Fig. 7.** Representative SYSWELD images showing cross-sections of the weld pool temperature for each weld condition, including a) GTAW root pass, b) first GMAW cover pass, c) second GMAW cover pass, and d) third GMAW cover pass.

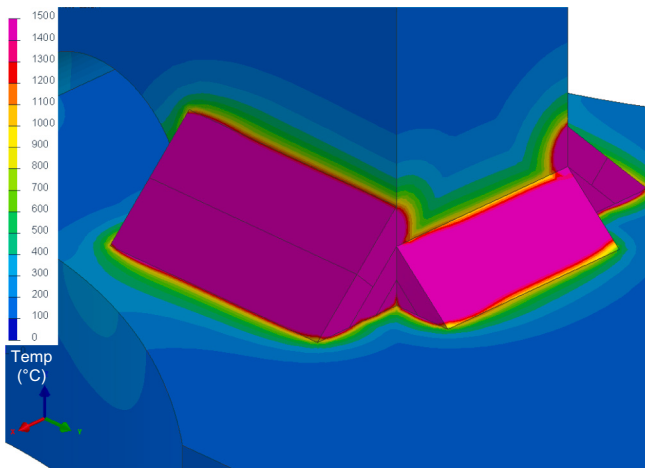


**Fig. 8.** Representative SYSWELD image showing the maximum temperature reached throughout the entire welding simulation.

2. Second optimization invoking a ‘robust’ least squares. The notion here is to keep a peak with relatively large intensity from dominating the residual by means of a loss function [27]. The loss function is

scaled in order to separate ‘weak’ and ‘strong’ peaks. The initial parameters are taken from the prior optimization with common strain.

3. Final optimization invoking the usual least squares but using initial parameters from robust least squares optimization.

A histogram of difference between the intensity-weighted average strain from the least squares fit and common strain fit are given in Fig. 3a for the  $\varepsilon_{yy}$  component at measurement locations adjacent to the two-pass weld (location discussed in more detail below). The differences were relatively small, being less than an order of magnitude compared to the peak residual strains developed in welding.

#### 2.3.1. Lattice parameter verification

The zero-strain lattice parameter ( $d$ -spacing) of the alloy was calculated and cross-checked using a series of line scans. First, a line scan of the YY strain component was performed on a high symmetry vector along the center axis of the un-welded reinforcement arch (see Fig. 2b, Specimen #2), where the strain is expected to be zero along this line (see Fig. 3b). The lattice parameter was adjusted until the strain was within  $1 \times 10^{-6}$ . As a cross check, a series of scans through the thickness of the large plates – checked on Specimen #1, the dog-bone shape of Specimen #2, and the dog-bone shape of Specimen #3 – were measured for the in-plane YY strain component. Assuming a biaxial stress state with

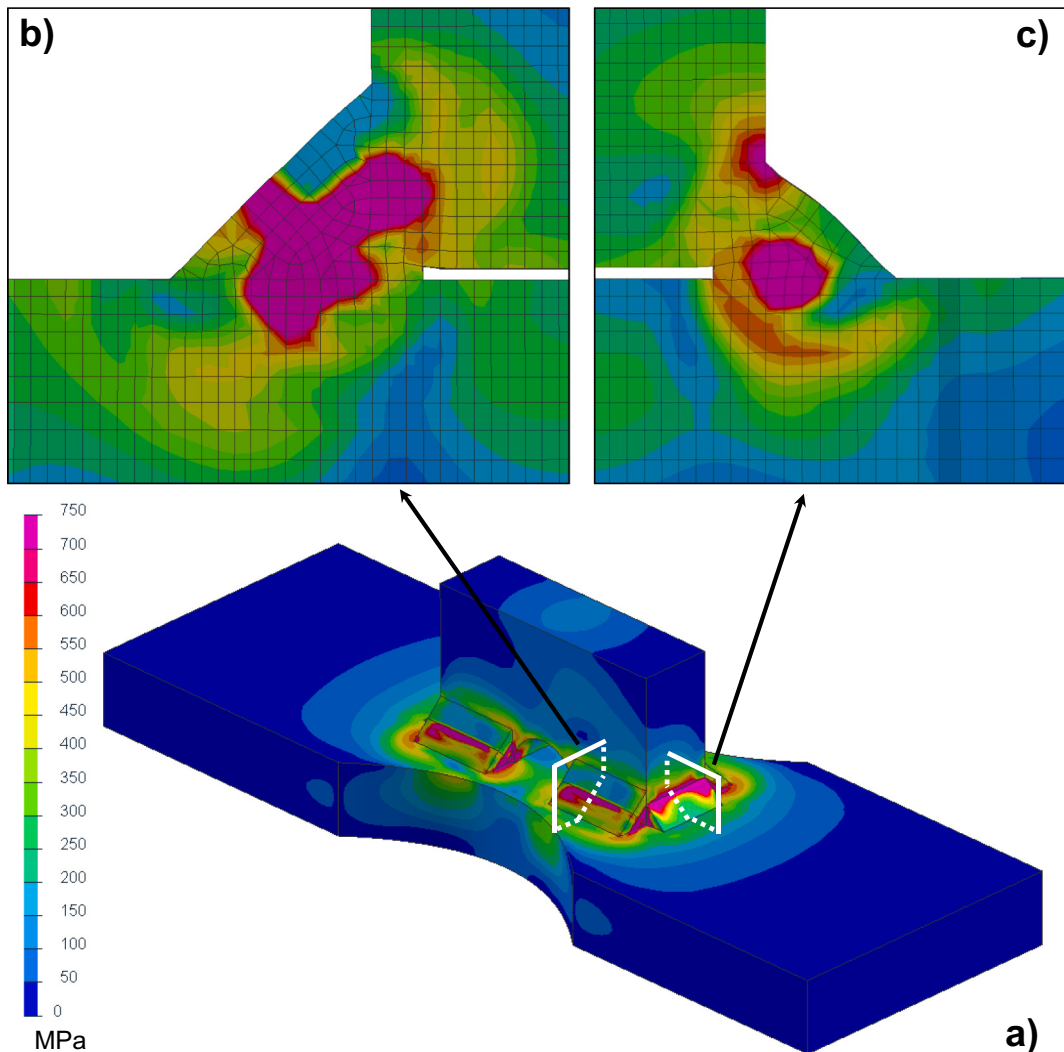


**Fig. 9.** SYSWELD images of the final stress state (Von Mises criteria) after the completion of welding and the cooling period to bring the piece back to room temperature, for the a) full weldment and cross-sections of the b) longitudinal and c) transverse joints.

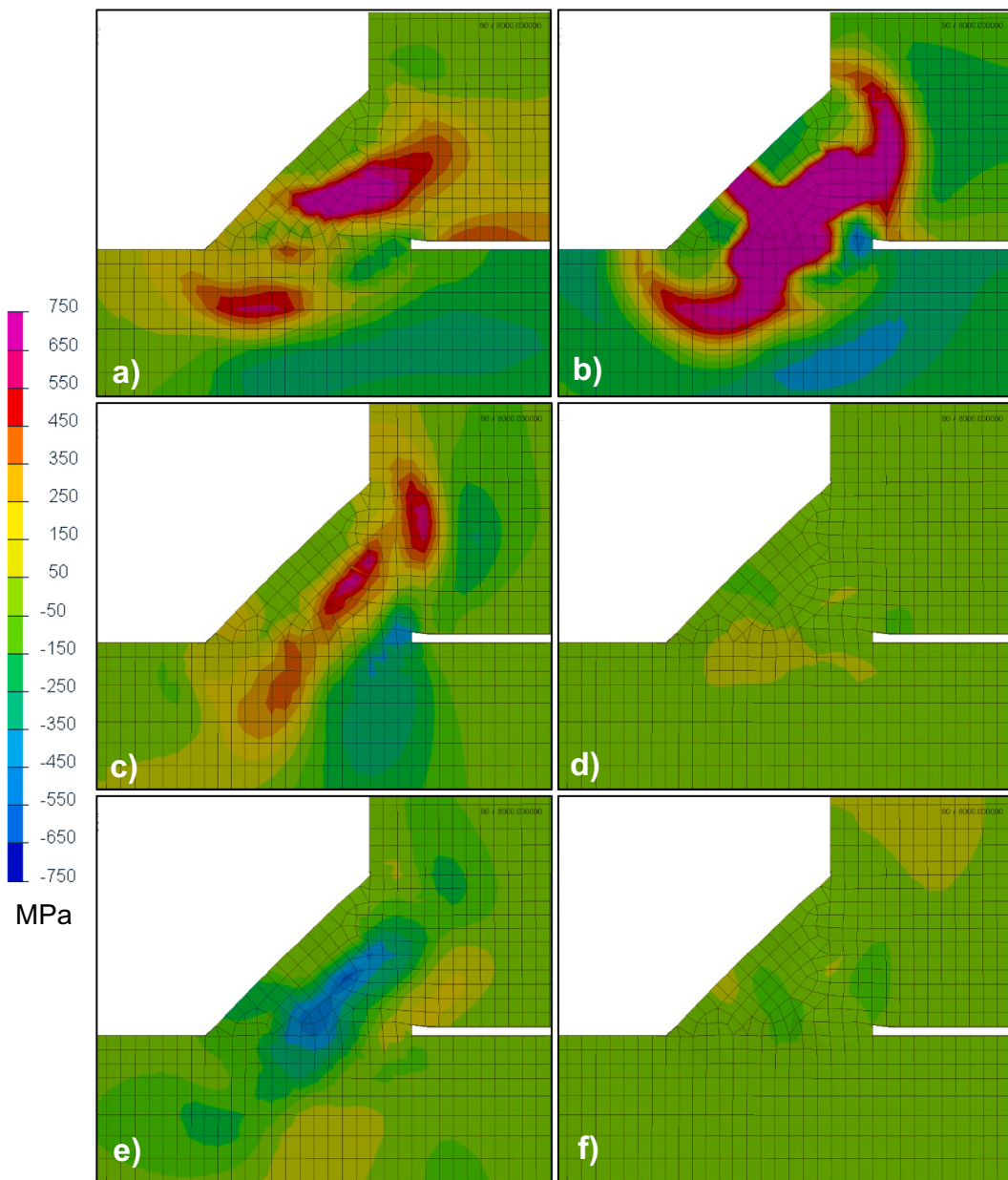


**Fig. 10.** Representative SYSWELD images showing cross-sections of the final first principle stress state for the longitudinal (4-pass) weld joint scenario for all directions: a) XX, b) YY, c) ZZ, d) XY, e) XZ, f) YZ.

balanced through-thickness tensile and compressive stresses in the rolled plate, the sum of the strains in the through-thickness direction for each line scan should be zero. The lattice parameter resulted in summed strains less than  $1 \times 10^{-4}$ , the resolution limit for the experimental conditions of this technique. Therefore, the lattice parameter of 2.8691 was determined to be reasonable. The plates were assumed to be compositionally uniform in the through-thickness direction for the purposes of this lattice parameter calibration.

#### 2.3.2. EDD measurement locations

The location of the EDD measurements was at the center cross-section of two different (but representative) weld joint types – longitudinal and transverse. Fig. 4 shows section cuts of the meshed CAD file highlighting the two different locations for the EDD measurements completed below those weld joints. This EDD data was used for V&V of the SYSWELD simulations.

### 3. Results and discussion

#### 3.1. Material properties

Table 2 shows a comparison of the measured chemical composition to that of specifications. The reported values for all elements except for carbon and sulfur are an average of twelve measurements; carbon and sulfur values were an average of six measurements. No individual measurement fell outside the specification range for any element. Table 3 shows the measured mechanical properties of the selected plate. There was not found to be a significant difference between the specimens tested longitudinally versus transverse in relation to the length of the plate. The HSLA-100 plate was found to meet the specified requirements in Tech Pub 300 [18].

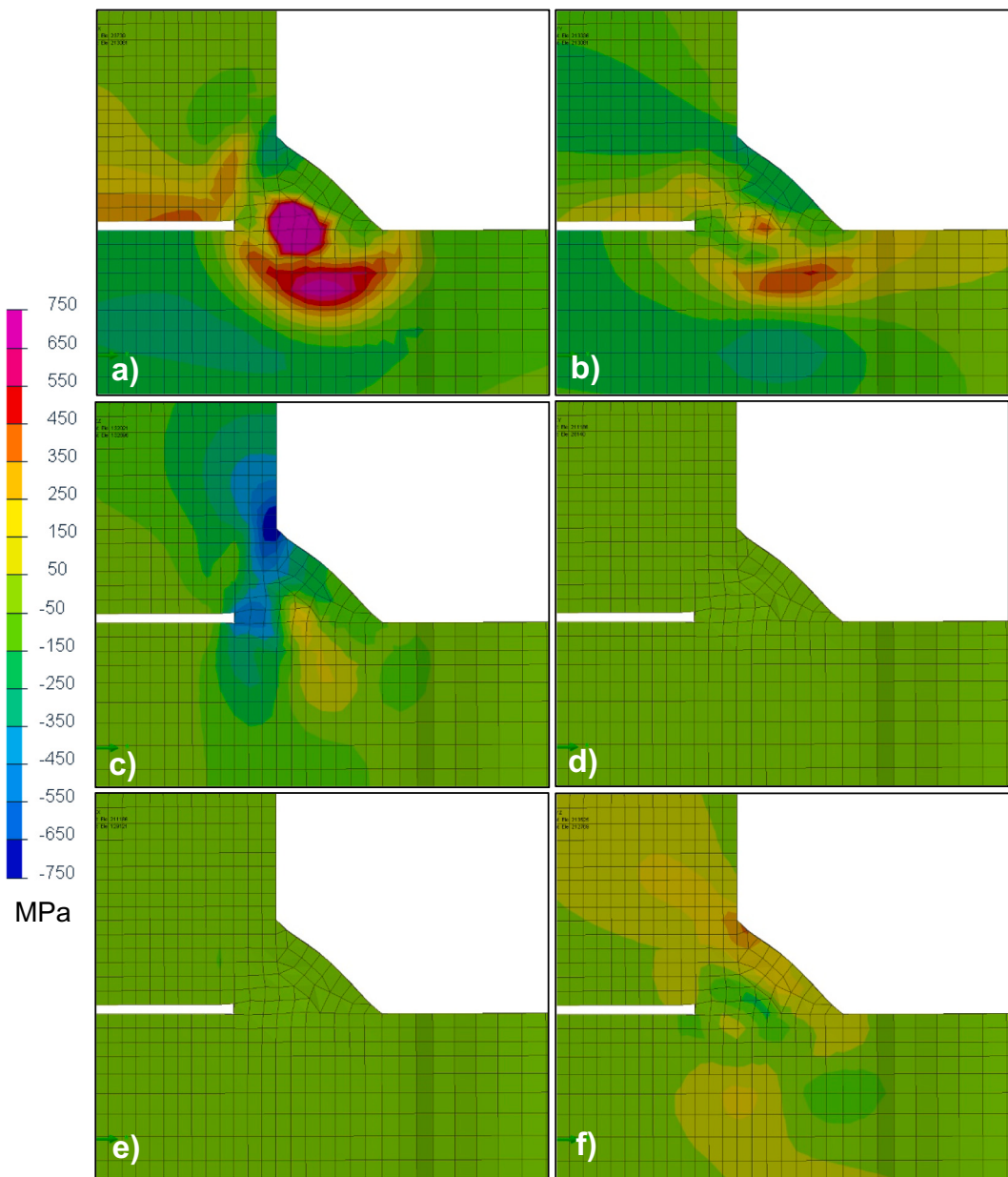


**Fig. 11.** Representative SYSWELD images showing cross-sections of the final first principle stress state for the transverse (2-pass) weld joint scenario for all directions: a) XX, b) YY, c) ZZ, d) XY, e) XZ, f) YZ.

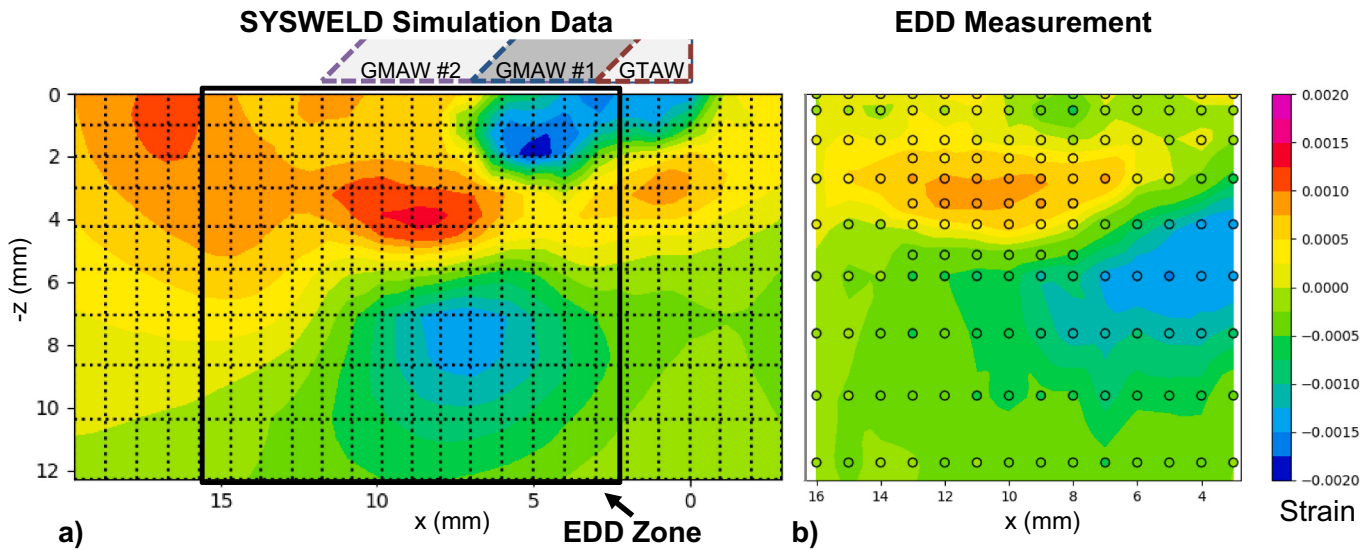
### 3.2. Representative weld cross-sections

Fig. 5 shows the cross-sections of the representative weld passes (not cross-sections of the actual Specimen #3 weldment) used for weld bead sizing during the FEA simulations. As expected, the GMAW covering passes were found to thermally overwhelm the GTAW root pass. Additionally, the penetration depth of each weld pass (particularly the first GMAW pass) helped to understand which elements to connect between the reinforcement arch and dog-bone shape in the FEA model. It should be noted that the transverse joints only had a root GTAW pass and covering GMAW pass, as shown in Fig. 5b, whereas the longitudinal joints had the root GTAW pass and three covering GMAW passes, as shown in Fig. 5c.

### 3.3. Weldment fabrication

As expected in the thick-plate (nominally 25.4 mm [1-in.])

weldment, there was little distortion noted. The most was a slight curvature, below 1 mm (0.04-in.), found in the dog-bone shape of Specimen #3 post-welding as shown in Fig. 6a. However, this slight lack of flatness was not found in the Specimen #2 cut shapes (dog-bone and arch) but was noted in Specimen #1 (incoming plate). This leads the authors to believe the non-flatness has origins in initial plate production, which was not included in the FEA simulations at this time. Follow-on work will investigate the effect of rolling and heat-treatment on the incoming FEA model used in welding simulation. However, because of the variability in the industrial processes, the author's believe the sister sample examination is valid to determine the trends across the fabrication process, despite any slight imprecision the lack of initial plate fabrication information (distortion and stress) that can be included in the welding simulation at this time.



**Fig. 12.** Comparison of strain map in the XX direction for the cross-section of the longitudinal (4-weld) joint for a) the calculated SYSWELD strain map compared to b) the EDD measurement strain map.

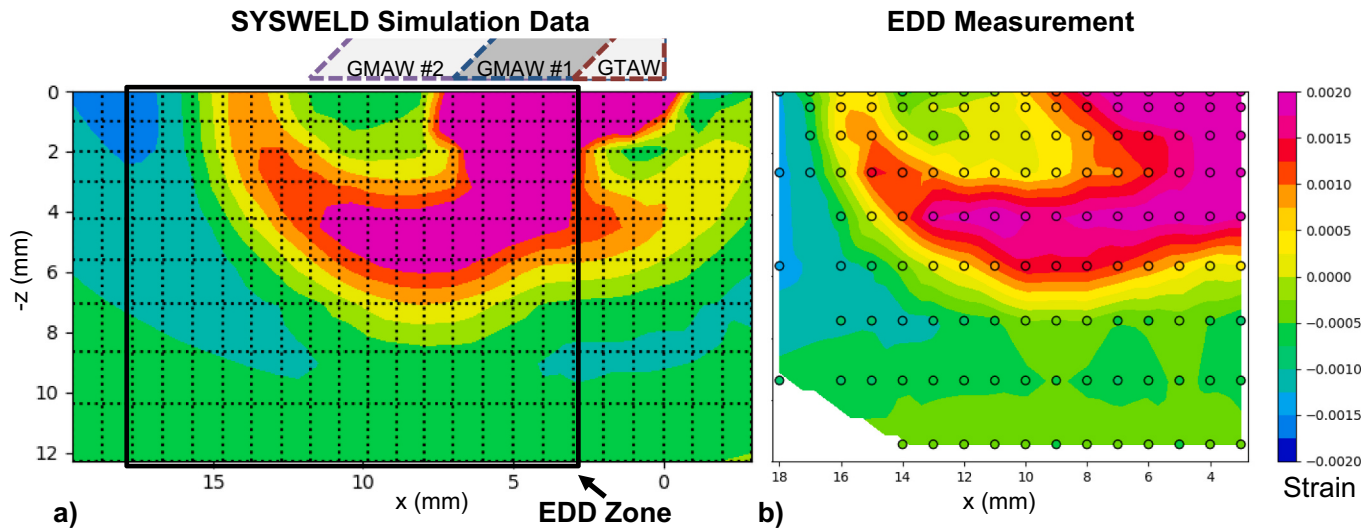


**Fig. 13.** Comparison of strain map in the YY direction for the cross-section of the longitudinal (4-weld) joint for a) the calculated SYSWELD strain map compared to b) the EDD measurement strain map.

### 3.4. Computational simulation

The SYSWELD simulations resulted in several thermo-physical and thermo-mechanical datasets that validated results from the physical fabrication. Fig. 7 shows the representative images of the melt pool for each weld pass condition at the center cross-section of the bead exhibiting the largest melt pool. It was found that the melt pool did not significantly change between the different beads at different locations on the weldment. This was expected due to the average welding parameters used during the FEA simulation. The melt pool sizes shown in Fig. 7 matched the expected weld bead width and penetrations shown in Fig. 5, which validates the simulation technique according to AWS A9.5 standards [23]. Fig. 8 shows the maximum temperature realized at every node throughout the entire simulation, highlighting that the entire weld zone was melted. The reverse side of the weldment exhibited similar thermal profiles. The thermal simulations also verified that the interpass temperature, 93–149 °C (200–300 °F), was maintained throughout the welding process, which matches that of the physical fabrication of

Specimen #3. The highest temperature for any node at the completion of the entire simulation (8000 s) was 22.9 °C (73.2 °F).

The FEA simulation results predicted there would be less than 0.52 mm (0.02-in.) distortion for any node at the completion of the simulation, as shown in Fig. 6b. Further examination showed that no node exhibited any additional distortion above 0.7 mm (0.03-in.) at any point within the entire weld simulation. The as-expected lack of distortion also serves as V&V for the simulation compared to the physical specimen, which also yielded little distortion as shown in Fig. 6a.

The FEA simulation results predicted the highest residual stress near the weldments, as shown in Fig. 9. Similar stress states were predicted for the reverse side of the weldment. A peak value of 700–750 MPa (102–109 ksi) was selected because the minimum yield strength of HSLA-100 plate material is 690 MPa (100 ksi). Fig. 9b–c shows additional images of cross-sections at the mid-point of the different weld joints, both longitudinal and transverse. As expected, the highest stress zones were found to be near the root of each welded joint.

For comparison to the X-ray measurements from CHESS, an

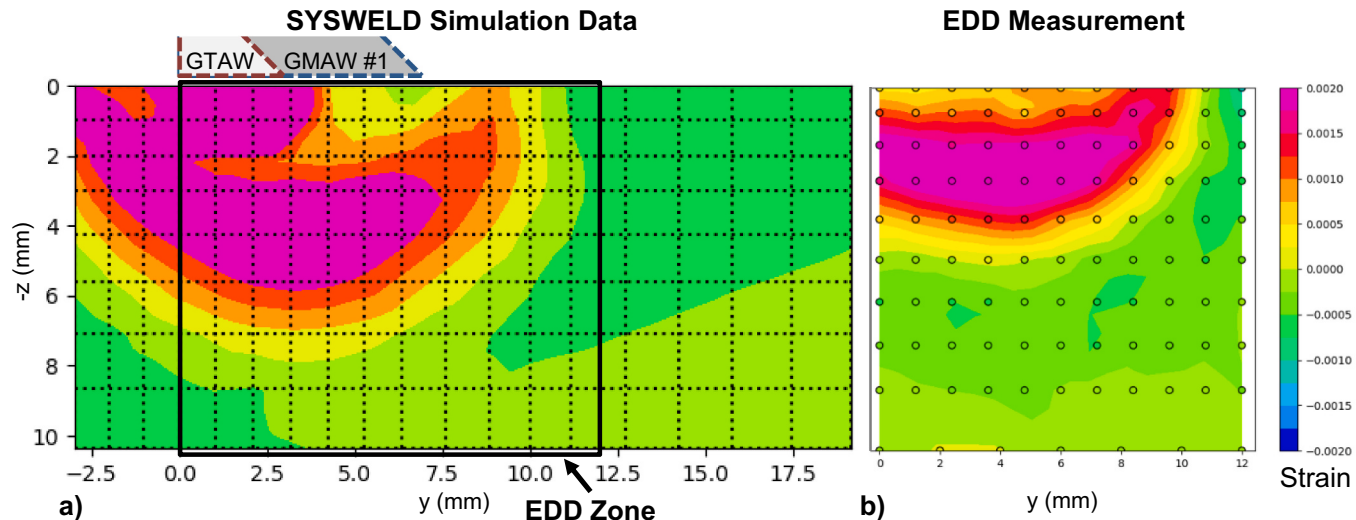


**Fig. 14.** Comparison of strain map in the XX direction for the cross-section of the transverse (2-weld) joint for a) the calculated SYSWELD strain map compared to b) the EDD measurement strain map.

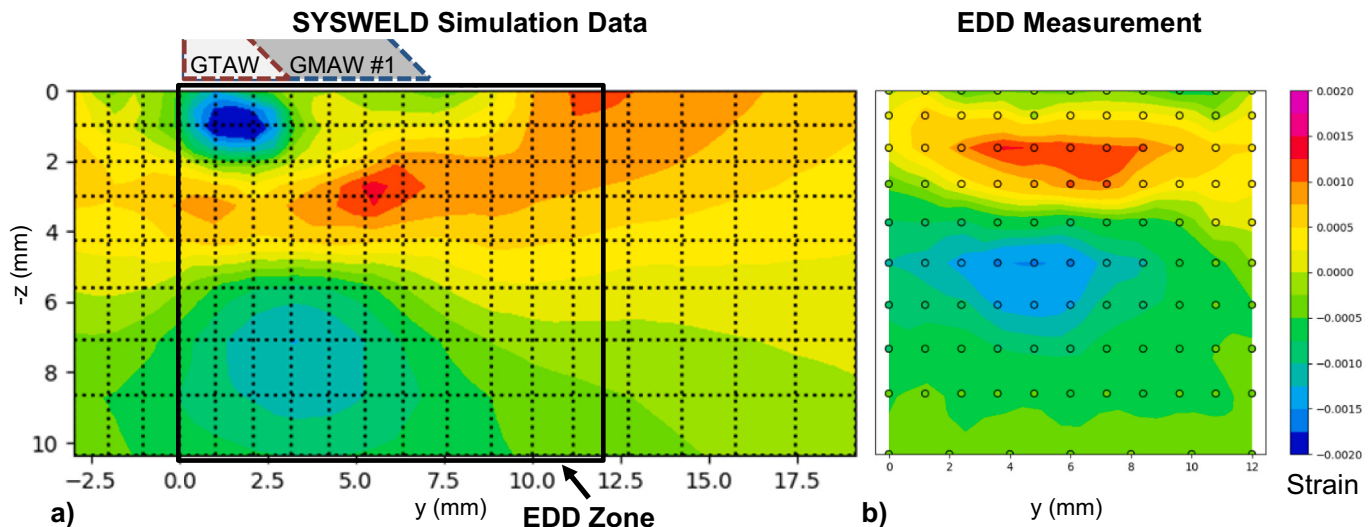


**Fig. 15.** Comparison of strain map in the YY direction for the cross-section of the transverse (2-weld) joint for a) the calculated SYSWELD strain map compared to b) the EDD measurement strain map.

examination of the residual stress across the six principle stress directions (XX, YY, ZZ, XY, XZ, YZ) was needed. Fig. 10 shows these results for the longitudinal (4-pass) weld joint, whereas Fig. 11 shows the results for the transverse (2-pass) weld joints. Note that the first principle stress values were predicted to be relatively consistent across the symmetric planes of the weldment, so only one representative cross-section is shown for each weld joint condition.

### 3.5. Strain measurement and comparison

Strain components measured through EDD are shown as contour maps for two strain components ( $\epsilon_{xx}$  and  $\epsilon_{yy}$ ) orthogonal to the weldment dimensions. Fig. 12 shows these results for the longitudinal (4-pass) weld joint in  $\epsilon_{xx}$ , Fig. 13 shows the longitudinal (4-pass) weld joint in  $\epsilon_{yy}$ , Fig. 14 shows the transverse (2-pass) weld joint in  $\epsilon_{xx}$ , and Fig. 15 shows the transverse (2-pass) weld joint in  $\epsilon_{yy}$ . The coordinate system for the EDD measurements matched that of the simulated weldment. In Figs. 12–15, the circle symbols in each EDD plot represent the specific

positions of the EDD measurements and are colored by their direct strain measurement. The contours between each circle are interpolated using the location-specific data at each EDD measurement point. For clarity of comparison, the black box in the SYSWELD simulation data maps represents the area where the EDD measurements were taken. The dashed outline of shapes above the SYSWELD simulation data maps show the relative location of the individual GTAW and GMAW passes for each joint scenario.

The SYSWELD simulation strains for the derived maps in Figs. 12–15 were calculated from the predicted first principle stress tensor (XX, YY, ZZ, XY, XZ, and YZ) at each node. Maps of those stress values were shown previously for both weld joint configurations in Figs. 10–11. The predicted nodal stress ( $\sigma$ ) was converted to strain ( $\epsilon$ ) using the isotropic form of Hooke's law:

$$\epsilon_{ij} = \frac{1}{E} [\sigma_{ij} - v(\sigma_{kk}\delta_{ij} - \sigma_{ij})] \quad (5)$$

where  $i, j$ , and  $k$  = directions in x,y,z space,  $E$  = elastic modulus (taken as

210 GPa [30.4 Msi] for steel),  $\nu$  = Poisson's ratio (taken as 0.33 for steel), and  $\delta$  = Kronecker delta (either 0 or 1).

The predicted strain from the FEA simulation to the EDD measurements was found to exhibit high correlation for all four scenarios. In particular, the shape and curvature correlation for  $\epsilon_{yy}$  of the longitudinal (4-weld) joint (Fig. 13) and  $\epsilon_{xx}$  of the transverse (2-weld) joint (Fig. 14) showed that the highest strain levels ( $>0.0015$ ) were being captured appropriately. These high tensile strains were likely caused by the shrinkage forces from weld metal solidification parallel to the welding direction of each joint and were expected. These high tensile strains were also likely to overwhelm any steel fabrication strains which evolved from the plate rolling, heat treatment, and cutting operations prior to welding, thus resulting in the best correlation between the FEA predictions and EDD measurements for those two scenarios.

While there was good agreement between the tensile strain zones in the  $\epsilon_{xx}$  of the longitudinal (4-weld) joint (Fig. 12) and  $\epsilon_{yy}$  of the transverse (2-weld) joint (Fig. 15), the highest strains ( $>0.0015$ ) were not realized. This is likely because these cross-sections ran orthogonal to the welding direction at each joint, and would have experienced much lower shrinkage forces. It was noted that a high compressive strain ( $>-0.0015$ ) was predicted immediately beneath the weld beads within the heat-affected zone (HAZ). However, the EDD measurements did not exhibit the same localized compression strain region. The authors believe this was the result of the modified chemistry from dilution of the filler metal into the base metal within the HAZ, which would result in a slight deviation in the d-spacing for that region relative to the rest of the steel plate. Further analysis is on-going.

Other minor differences between the EDD measurements and the FEA predictions are attributed to the lack of fabrication process (*i.e.*, plate rolling, heat treatment, and cutting) information able to be inserted into the FEA simulation as of this writing. Follow-on work to examine the stress state of the incoming plate, to include the effects of the fabrication process, is on-going. A similar examination of EDD measurements compared to FEA simulations of in-coming plate and the effects of each fabrication step is on-going.

#### 4. Conclusions

This materials-informed digital twin effort leveraging ICME techniques seeks to serve as the basis for inclusion of materials processing data into structural evaluation and mechanical performance. A set of “sister-samples” to represent various steps in the fabrication process was produced from a single plate of 25.4 mm (1-in.) thick HSLA-100 steel. Specimen #1 represented incoming rolled plate, Specimen #2 represented cut pieces, and Specimen #3 represented the final welded structure. Long-term efforts seek to understand the evolution and distribution of residual stress from the entire fabrication process through FEA simulations and EDD measurements, but this report focused only on data associated with the final weldment, Specimen #3.

Initial FEA analysis of the weldment showed high tensile stresses near the weld passes in the heat-affected zone (HAZ), as expected. Validation of the predicted strain within the dog-bone shape showed high correlation between the measured EDD data and the FEA predictions, particularly for the high strain ( $>0.0015$ ) fields of first principle strain vectors measured parallel to each welding pass. These high strains are likely the result of the shrinkage forces associated with weld metal solidification and cooling. Follow-on work will investigate the inclusion of other fabrication-based strains (*i.e.*, plate rolling, heat treatment, and cutting) into the FEA analysis, plus establish the mechanical performance (*e.g.*, fatigue) of the final weldment in comparison to FEA analysis with and without the included fabrication stresses.

#### Funding

The NSWCCD work was funded in through the Naval Innovative Science and Engineering (NISE) Research and Development program at

NSWCCD. The work at CHESS was supported by the Air Force Research Laboratory (AFRL) under award FA8650-19-2-5220.

#### Declaration of competing interest

The authors declare that they have no known competing financial interests or personal relationships that could have appeared to influence the work reported in this paper.

#### Acknowledgements

The authors would like to thank Carrie Davis, Richard Gins, Jimmy Hayden, Shawn Robinson, and Dan Root at NSWCCD as well as Arthur Woll, Matt Miller, Darren Pagan, Peter Ko, and Chris Budrow at CHESS for their technical assistance in the completion of this work.

#### Appendix A. Supplementary data

Supplementary data to this article can be found online at <https://doi.org/10.1016/j.jmapro.2021.11.057>.

#### References

- [1] Lawrence F, Burk J, Yung J. Influence of residual stress on the predicted fatigue life of weldments. In: Residual stress effects in fatigue (ASTM STP 776). West Conshohocken, PA: ASTM International; 1982. p. 33–43.
- [2] Webster GA, Ezeilo AN. Residual stress distributions and their influence on fatigue lifetimes. Int J Fatigue 2001;23:S375–83.
- [3] Barsoum Z, Barsoum I. Residual stress effects on fatigue life of welded structures using LEFM. Eng Fail Anal 2009;16(1):449–67.
- [4] Huang TD, Dong P, Decan L, Harwig D, Kumar R. Fabrication and engineering technology for lightweight ship structures, part 1: distortions and residual stresses in panel fabrication. J Ship Prod 2004;20(1):43–59.
- [5] Committee on Integrated Computational Materials Engineering - National Research Council. Integrated computational materials engineering: a transformative discipline for improved competitiveness and national security. Washington, D.C: National Academies Press; 2008.
- [6] Integrated computational materials engineering (ICME): implementing ICME in the aerospace, automotive, and maritime industries. Warrendale, PA: "The Minerals, Metals, and Materials Society (TMS); 2013.
- [7] Levieil B, Bridier F, Doudard C, Thevenet D, Calloch S. User influence on two complementary residual stress determination methods: contour method and incremental X-ray diffraction. Exp. Mech. 2016;56:1641–52.
- [8] Withers PJ, Turski M, Edwards L, Bouchard PJ, Buttle DJ. Recent advances in residual stress measurement. Int J Press Vessel Pip 2008;85(3):118–27.
- [9] Pagliaro P, Prime MB, Robinson JS, Clausen B, Swenson H, Steinigz M, Zuccarello B. Measuring inaccessible residual stresses using multiple methods and superposition. Exp Mech 2011;51:1123–34.
- [10] Wan Y, Jiang W, Li J, Sun G, Kim D-K, Woo W, Tu S-T. Weld residual stresses in a thick plate considering back chipping: neutron diffraction, contour method and finite element simulation study. Mater Sci Eng A 2017;699:62–70.
- [11] Phan TQ, Stantza M, Hill MR, Gnaupel-Herold TH, Heigel J, D'Elia CR, DeWalid AT, Clausen B, Pagan DC, Ko KP, Brown DW, Levine LE. Elastic residual strain and stress measurements and corresponding part deflections of 3D additive manufacturing builds of ING25 AM-bench artifacts using neutron diffraction, synchrotron X-ray diffraction, and contour method. Integrating Mater Manuf Innov 2019;8:318–34.
- [12] Zhang Y, Ganguly S, Stelmukh V, Fitzpatrick ME, Edwards L. Validation of the contour method of residual stress measurement in a MIG 2024 weld by neutron and synchrotron X-ray diffraction. J Neutron Res 2006;11(4):181–5.
- [13] Mach JC, Budrow CJ, Pagan DC, Ruff JP, Park J-S, Okasinski J, Beaudoin AJ, Miller MP. Validating a model for welding induced residual stress using high-energy X-ray diffraction. JOM 2017;69(5):893–9.
- [14] Mach JC, Gales C, Okasinski J, Budrow CJ, Beaudoin AJ, Swartz K, Miller MP, Gnaupel-Herold T, Park J-S. FD&E total life T-sample residual stress analytical predictions and measured results. SAE Technical Paper; 2019.
- [15] Prime MB. Residual stresses measured in quenched HSLA-100 steel plate. In: Proceedings of the SEM annual conference and exposition on experimental and applied mechanics; 2005.
- [16] Bahadur A, Kumar BR, Chowdhury SG. Effect of thermomechanical treatment on X-ray elastic constants and residual stresses in HSLA-100 steel. J Nondestruct Eval 2005;22(2):53–62.
- [17] Duch JE, DuPont JN. Effect of multiple weld thermal cycles on HSLA-100 steel the microstructure and mechanical properties of high-strength low-alloy steel during multipass welding. Weld J 2019;98(3):88S–98S.
- [18] NAVSEA. T9074-BD-GIB-010/300 (Rev. 2), "Base materials for critical applications: requirements for low alloy steel plate, forgings, castings, shapes, bars, and heads of HY-80/100/130 and HSLA-80/100. Washington, D.C: NAVSEA; 2012.

- [19] ASTM E415-17. Standard test method for analysis of carbon and low-alloy steel by spark atomic emission spectrometry. West Conshohocken, PA: ASTM International; 2017.
- [20] ASTM E1019-18. Standard test methods for determination of carbon, sulfur, nitrogen, and oxygen in steel, iron, nickel, and cobalt alloys by various combustion and inert gas fusion techniques. West Conshohocken, PA: ASTM International; 2018.
- [21] ASTM A370-18. Standard test methods and definitions for mechanical testing of steel products. West Conshohocken, PA: ASTM International; 2018.
- [22] Goldak J, Chakravarti A, Bibby M. A new finite element model for welding heat sources. Metall Trans B 1984;15:299–305.
- [23] AWS A9.5. Guide for verification and validation in computational weld mechanics. Miami, FL: American Welding Society; 2013.
- [24] DuPont J, Marder A. Thermal efficiency of arc welding processes. Weld J 1995;74(12). pp. 406–416-s.
- [25] ESI Software. Visual weld 14.5. 2019. Accessed: 6 September.
- [26] Visual environment 14.5, "TRIP 700Z," ESI material database. 2019.
- [27] Virtanen P, Gommers R, Oliphant T, Hoyerland M, Reddy T, Cournapeau D, 1.0 SciPy Contributors. SciPy 1.0: fundamental algorithms for scientific computing in python. Nat Methods 2020;17:261–72.
- [28] J. Vernier , "HEXRD," [Online]. Available: <https://github.com/joelvbernier/hexrd.git>.
- [29] Czuryca EJ. Development of low-carbon, copper-strengthened HSLA steel plate for naval ship construction. Bethesda, MD: David Taylor Research Center; 1990.